

RSC Advances



This is an *Accepted Manuscript*, which has been through the Royal Society of Chemistry peer review process and has been accepted for publication.

Accepted Manuscripts are published online shortly after acceptance, before technical editing, formatting and proof reading. Using this free service, authors can make their results available to the community, in citable form, before we publish the edited article. This *Accepted Manuscript* will be replaced by the edited, formatted and paginated article as soon as this is available.

You can find more information about *Accepted Manuscripts* in the [Information for Authors](#).

Please note that technical editing may introduce minor changes to the text and/or graphics, which may alter content. The journal's standard [Terms & Conditions](#) and the [Ethical guidelines](#) still apply. In no event shall the Royal Society of Chemistry be held responsible for any errors or omissions in this *Accepted Manuscript* or any consequences arising from the use of any information it contains.

Designing and optimizing a stirring system for a cold model of lithium electrolysis cell based on CFD simulations and optical experiments

*Ze Sun**, Haiou Ni, Hang Chen, Suzhen Li, Guimin Lu and Jianguo Yu

National Engineering Research Center for Integrated Utilization of Salt Lake Resource,

East China University of Science and Technology,

Shanghai 200237, People's Republic of China

* To whom correspondence should be addressed. Ze Sun: Tel: 86-21-64252826. Fax: 86-21-64250981.
E-mail: zsun@ecust.edu.cn.

ABSTRACT: In electrolysis lithium industry, liquid lithium metal and chloride gas need to separate quickly because of recombination of lithium and chloride. A new stirring system can help to separate liquid metal and chloride in the lithium electrolysis cell. The stirring system was tried in the cold model to get the right parameters. Computational Fluid Dynamics (CFD) and Particle Image Velocimetry (PIV) were both employed to design and optimize the device parameters which included impeller type, diameter, position and rotational speed. PIV tests and CFD models validation were conducted in a cylinder stirred tank. Different turbulence models were applied and the standard k- ϵ model was considered as the most suitable one. The results show that: the propeller agitator with low blades number and low installation position were advantageous to the lithium collection. The impeller diameter and rotational speed have positive effects on the expected flow field. The simulation results were applied in cold model experiments, which shows simulations are correct and can be used in real separator designing.

KEYWORDS: lithium electrolysis, stirred system, CFD, optimization.

1. Introduction

Lithium is an important strategic resource which is widely used in alloys, batteries, thermonuclear fusion, organic synthesis, etc^{1,2}. Now, the industrial production of lithium metal relies on the molten salt electrolysis. However, there are two main problems in the industrial production: high energy consumption and low product purity³. Up to now, different types of electrolytic cell have been proposed to solve these problems⁴⁻⁶. Through comprehensive comparison of the different structure cells, a German electrolysis cell⁵ was considered to be a potential one, shown in figure 1. It has a stirring system to separation of lithium and chloride to improve electrolysis efficiency and product purity, because the system can separate lithium and chloride efficiently by providing negative pressure through a small tube. So, a good stirring system is the key point for this type electrolysis cell.

In order to design a good stirring system, simulation and experiment are main two ways used by researchers. Simulation is carried out through Computational Fluid Dynamics (CFD), which is widely used in the researches about hydrodynamics^{7,8}. In CFD procedure for stirred tanks, two commonly models for rotation characteristics are Multiple Reference Frames (MRF) and Sliding Mesh (SM)⁹. The MRF model has been found to give similar results using less computational expense comparing with SM impeller rotation model for the steady-state simulation of stirred tanks.^{10,11} For the MRF model, steady-state calculations are performed with a rotating reference frame in the impeller region and a stationary reference frame in the outer region. In this way, the effects of the blade rotation are accounted for by virtue of the frame of reference, allowing for explicit modelling of the impeller geometry^{9,12}. The related researches about the impeller configuration has been reported, especially the Ruston turbine which has the least power number. The impeller type, configuration, size and placed position have obvious effects on the power number or other flow field physical quantities¹³⁻¹⁵. And the geometry of the vessel is studied as well. The results indicate that the number of baffles has no effect on the maximum turbulence

dissipation rate, either as an independent variable, or in the form of interaction with other geometric variables¹⁶.

In simulation process, rotation is one of key points, and turbulence is the other key point. In most of stirred tanks, turbulence is a common phenomenon because of high speed of agitator. Right turbulent model can save simulation cost and get accurate results. For turbulent flow in stirred tanks, Reynolds-Averaged Navier-Stokes (RANS) and Large Eddy Simulation (LES) are in practice, however, LES is usually used in small scale simulation for its high demand of computational resources^{17,18}. The k-epsilon model is the most established turbulence model in RANS for engineering flows and has been widely used for modelling turbulent flow in stirred tanks^{19,20}. Abujelala²¹ and Armentante²² discussed accuracy of k-e model and other researchers^{23,24} compared flow predictions in stirred tanks using variations of the k-e model such as Renormalized Group (RNG) k-e and standard k-e models. Generally, the different variations have resulted in only slight changes in turbulence predictions, and in some cases the standard model gave superior results.

Although CFD simulation did effective designing and optimization in many fields²⁵⁻²⁸, experiment is still the most reliable way to get accurate results or credible validation for mathematical model^{29,30}. Laser Doppler Velocimetry (LDV) and Particle Image Velocimetry (PIV) are the main means of flow field measurements for stirred tanks now³¹⁻³³. These two equipments have their own advantages: the former is single-point measurement and provides more flow field information while PIV is multi-dimensional measurement with bigger testing area³⁴. The main problem of PIV measurement is the resolution which is related to the captured image area. This problem can be resolved with large PIV method which is proposed by Sheng and Drumm^{35,36}. Now, three-dimension measurements also appear to provide much more real flow field information³⁷. In PIV procedure, the density of particle in an image is the most important factor. P. Pianko-Oprych³⁸ did many experiments to get best density of particles for spatial resolution. He and Deshpande³⁹ showed 5-15 particles in unit searching area can result in best resolution. In order to get the best results, Khan⁴⁰ proposed angle-resolved stereo-PIV to study different

angle of impeller, and Sharp⁴¹ studied average treatment for steady flow field in stirred tanks. In practice, average is an effective and high efficiency way for steady stirred tanks, comparing with angle-resolved stereo-PIV is more effective for time dependent flow field.

In all, CFD and PIV have their own advantages. To combine PIV and CFD to study the flow field of stirred tank can use their own advantages and overcome their own disadvantages. This combination can let each method to validate the other. So, in this study, CFD and PIV were both employed to optimize a cold model of the stirred device in lithium electrolysis cell which is little reported in literatures. The accuracy of the CFD model was validated in an ordinary stirred tank with the help of PIV. The geometry and operation parameters of the stirred device including impeller type, diameter, position and rotational speed were optimized with the commercial software Fluent 6.3. Parts of optimized results were compared to the PIV results again to validate the simulation further. At the end of paper, cold model experiments were carried out to validate the designing and optimization.

2. Experimental Instrumentation

2.1. Introduction of lithium and chloride separation device

The details of lithium and chloride separation device's structure are shown in Fig. 1. In this figure, the main liquid are electrolyte including KCl, NaCl, LiCl et al. Liquid lithium flows on the surface of electrolyte for its density is smaller than that of electrolyte. Liquid lithium released from cathode and chloride released from anode go up along electrodes to the surface of electrolyte, and they will recombine into LiCl again if liquid lithium is not removed in time. So the stirring system is installed to separate lithium. An impeller is utilized to generate negative pressure in the collection chamber, shown in the right of Fig. 1. Then the liquid lithium will be transferred from electrolysis chamber to collection chamber due to pressure differences. Hence, the design and optimization of such a collection device is especially important.

(Inserting Figure 1 here)

2.2. Experimental device

In order to design a collection device shown in figure a, the preliminary model validation for PIV was carried out in a stirred cylindrical tank of diameter $t = 240$ mm. The vessel was filled with tap water and the liquid height h was 200 mm. Four baffles were mounted averaged around the cylindrical vessel to eliminate vortex. Their width B was one tenth of the vessel diameter. All of the vessel and baffles were made of polymethyl methacrylate. The cylindrical stirred tank was located in a square glass vessel. Tap water was also injected into the square vessel to minimize the effect of optical refraction. A four-blades propeller of diameter $d = 100$ mm was employed in this test. The impeller blade and disk thickness was 2 mm. The space $c = h/3$ was employed between the bottom of the vessel and the impeller disk plane. The impeller counterclockwise rotational speed n was set to be 150 rpm to generate an obvious axial flow. Fig 2.a is a simple schematic diagram.

(Inserting Figure 2 here)

The stirred device in electrolysis cell was the emphasis in this research. It was not necessary to model the whole electrolysis cell. Proper simplification was essential and reasonable. Fig 2.b shows the simplified device, and its detailed geometry parameters are shown in Tab 1. In fact, the immersed internal was a tube which consists of three parts: a large pipe, a small pipe and a transition pipe. All of the components were made of glass to ensure enough transparence. The space $C = 95$ mm was employed between the bottom of the vessel and the internal. A three-blades propeller of diameter $D = 100$ mm and rotational speed $N = 300$ rpm was installed in the central of the large pipe while the optimization object focused on the axial velocity magnitude in the small pipe.

(Inserting Table 1 here)

2.3. Measurement instrument

A 2D PIV (TSI) was employed for the experiments concerning the flow field in this study. Fig 3 is the schematic diagram of the PIV system. The fluid was seeded with 10 μm neutrally hollow glass spheres which had excellent following performance. The pulse laser (Continuum) provided sheet laser to illuminate the glass spheres flowing with the fluid. The illuminated light was 1 mm thick, and the wavelength was 532 nm. A Charge Coupled Device (CCD) camera (Nikon 4M) was located vertical to the laser plane to capture the lighted particles. The particles were recorded twice at the time t and $t+\Delta t$ respectively. The coherence between the laser pulse and the digital camera at different time was realized with the help of the synchronizer. According to the recorded particle information, the corresponding software Insight 3G calculated the physical quantities of the flow field based on the cross-correlation processing with the interrogation cell sizes of 32 pixels. At the same time, an overlapping of 50% was employed for the processing. In addition, the number of captured images was one of the most important operation parameters³⁸. Its effect on results' accuracy was considered.

(Inserting Figure 3 here)

3. Mathematical and Physical Model

3.1. Mathematical model

The flow of the stirred tank was simulated with a single-phase model. The minimum Reynolds number of 15923 indicated that the turbulence model must be adopted in this study. The main governing equations of continuity and momentum equations are written as follows:

$$\frac{\partial \rho}{\partial t} + \frac{\partial p}{\partial x_i} (\rho u_i) = 0 \quad \text{Equation 1}$$

$$\frac{\partial(\rho u_i)}{\partial t} + \frac{\partial}{\partial x_j}(\rho u_i u_j) = -\frac{\partial p}{\partial x_i} + \frac{\partial}{\partial x_j} \left[\mu \left(\frac{\partial u_i}{\partial x_j} + \frac{\partial u_j}{\partial x_i} \right) \right] + \frac{\partial}{\partial x_j} (-\rho \overline{u'_i u'_j}) \quad \text{Equation 2}$$

For the velocity components:

$$u_i = \overline{u_i} + u'_i \quad \text{Equation 3}$$

Where $\overline{u_i}$ is the mean velocity and u'_i is the fluctuating velocity. The difficulty in equation solution procedure focus on the Reynolds stress term $-\overline{u_i u_j}$. The Reynolds averaged numerical simulation (RANS) employs models based on Boussinesq approach (k-ε models) and Reynolds stress transport models (Reynolds stress model) to close equation 2. It provides effective ways to balances the contradiction between prediction accuracy and computational cost.

The Boussinesq hypothesis adopts an isotropic turbulence viscosity μ_t to close the Reynolds stress term. The expression is shown in equation 4. Standard, RNG, Realizable k-ε models belong to this type.

$$-\overline{\rho u'_i u'_j} = \mu_t \left(\frac{\partial u_i}{\partial x_j} + \frac{\partial u_j}{\partial x_i} \right) - \frac{2}{3} \left(\rho k + \mu_t \frac{\partial u_k}{\partial x_k} \right) \delta_{ij} \quad \text{Equation 4}$$

The standard k-ε model calculates the turbulence viscosity μ_t with the turbulence kinetic energy k and turbulence dissipation ε which are calculated from the following transport equations:

$$\mu_t = \rho C_\mu \frac{k^2}{\varepsilon} \quad \text{Equation 5}$$

$$\frac{\partial}{\partial t}(\rho k) + \frac{\partial}{\partial x_i}(\rho k u_i) = \frac{\partial}{\partial x_j} \left[\left(\mu + \frac{\mu_t}{\sigma_k} \right) \frac{\partial k}{\partial x_j} \right] + G_k + G_b - \rho \varepsilon - Y_M + S_k \quad \text{Equation 6}$$

$$\frac{\partial}{\partial t}(\rho \varepsilon) + \frac{\partial}{\partial x_i}(\rho \varepsilon u_i) = \frac{\partial}{\partial x_j} \left[\left(\mu + \frac{\mu_t}{\sigma_\varepsilon} \right) \frac{\partial \varepsilon}{\partial x_j} \right] + C_{1\varepsilon} \frac{\varepsilon}{k} (G_k + C_{3\varepsilon} C_b) - C_{2\varepsilon} \rho \frac{\varepsilon^2}{k} + S_\varepsilon \quad \text{Equation 7}$$

Where G_k and G_b represent the generation of turbulence kinetic energy due to the mean velocity gradients and buoyancy, respectively. Y_M represents the contribution of the fluctuating dilatation in compressible turbulence to the overall dissipation rate. The default value of the model constants are $C_{1\varepsilon}=1.44$, $C_{2\varepsilon}=1.92$, $C_\mu=0.09$. The constant turbulent Prandtl numbers for k and ε are $\sigma_k=1.0$, $\sigma_\varepsilon=1.3$.

The Re-normalization Group (RNG) k - ε model was derived based on a statistical technique called renormalization group theory. It has the same model equations as the standard k - ε model except the main difference in the dissipation rate transport equation where an additional term R_ε is added to increase the accuracy for rapidly strained flows. The variable Prandtl number and effective viscosity are also adopted to improve its performance. Thus, it is more accurate and reliable for a wider class of flows than the standard k - ε model.

$$\frac{\partial}{\partial t}(\rho\varepsilon) + \frac{\partial}{\partial x_i}(\rho\varepsilon u_i) = \frac{\partial}{\partial x_j} \left[\alpha_\varepsilon \mu_{\text{eff}} \frac{\partial \varepsilon}{\partial x_j} \right] + C_{1\varepsilon} \frac{\varepsilon}{k} (G_k + C_{3\varepsilon} C_b) - C_{2\varepsilon} \rho \frac{\varepsilon^2}{k} - R_\varepsilon + S_\varepsilon \quad \text{Equation 8}$$

The realizable k - ε model differs from the standard k - ε model in two ways: the turbulence viscosity involving a variable C_μ and improved dissipation rate transport equation evolved from the exact dynamic equation of the mean-square vorticity fluctuation.

$$C_\mu = \frac{1}{A_0 + A_S \frac{kU^*}{\varepsilon}} \quad \text{Equation 9}$$

$$\frac{\partial}{\partial t}(\rho\varepsilon) + \frac{\partial}{\partial x_j}(\rho\varepsilon u_j) = \frac{\partial}{\partial x_j} \left[\left(\mu + \frac{\mu_t}{\sigma_\varepsilon} \right) \frac{\partial \varepsilon}{\partial x_j} \right] + \rho C_1 S \varepsilon - \rho C_2 \frac{\varepsilon^2}{k + \sqrt{v\varepsilon}} C_{1\varepsilon} \frac{\varepsilon}{k} C_{3\varepsilon} C_b + S_\varepsilon \quad \text{Equation 10}$$

In equation 10, the absence of G_k better represents the spectral energy transfer and the destruction term on the right side does not have any singularity. It has better performance than traditional k - ε models in many cases including rotating homogeneous shear flows, boundary layer flows and separated flows.

Although k - ε models have many advantages, their application is limited due to the isotropic assumption in the turbulent viscosity. The alternative approach is to solve transport equations for each of the terms in the Reynolds stress tensor, which is well known as Reynolds Stress Model (RSM). Seven additional transport equations are required to be solved in three dimensional simulations. The exact Reynolds stress transport equation is written as follows:

$$\frac{\partial}{\partial t}(\rho \overline{u'_i u'_j}) + \frac{\partial}{\partial x_k}(\rho u_k \overline{u'_i u'_j}) = D_{T,ij} + D_{L,ij} + P_{ij} + G_{ij} + \phi_{ij} + \varepsilon_{ij} + F_{ij} + S \quad \text{Equation 11}$$

Where the two terms on the left are the local time derivative and convection, respectively. The right terms $D_{T,ij}$, $D_{L,ij}$, P_{ij} , G_{ij} , Φ_{ij} , ε_{ij} , F_{ij} , S represent the turbulent diffusion, molecular diffusion, stress production, buoyancy production, pressure strain, dissipation, production by system rotation, and additional source term. Among all of them, $D_{L,ij}$, P_{ij} , F_{ij} do not require any modeling while different modeling assumptions are employed to close the terms of $D_{T,ij}$, G_{ij} , Φ_{ij} and ε_{ij} . Because the effects of streamline curvature, swirl, rotation, and rapid changes in strain rate are considered, the RSM has greater potential to predict complex flow accurately, especially the anisotropic flows.

For rotation characteristics, Multiple Reference Frames (MRF) of steady-state calculations are performed with a rotating reference frame in the impeller region and a stationary reference frame in the outer region. In this way, the effects of the blade rotation are accounted for by virtue of the frame of reference, allowing for explicit modelling of the impeller geometry. MRF models in Fluent software are expressed by two ways, relative velocity formulation and absolute velocity formulation. The paper used the latter, and the governing equations are written by follows:

Conservation of mass:

$$\frac{\partial \rho}{\partial t} + \nabla \cdot \rho \vec{v}_r = 0 \quad \text{equation 12}$$

Conservation of momentum:

$$\frac{\partial}{\partial t} \rho \vec{v} + \nabla \cdot (\rho \vec{v}_r \vec{v}) + \rho [\bar{\omega} \times (\vec{v} - \vec{v}_r)] = -\nabla p + \nabla \cdot \bar{\tau} + \vec{F} \quad \text{equation 13}$$

Where $\bar{\omega}$ is the angular velocity, \vec{v} is the absolute velocity (the velocity viewed from the stationary frame), \vec{v}_r is the relative velocity (the velocity viewed from the moving frame), \vec{F} is source term, $\bar{\tau}$ is expressed by equation 14.

$$\bar{\tau} = \mu \left[(\nabla \vec{v} + \nabla \vec{v}^T) - \frac{2}{3} \nabla \cdot \vec{v} I \right] \quad \text{equation 14}$$

where I is the unit tensor.

3.2. Numerical simulation strategies

The simulation model of the stirred tank was established in CFD software. The size of the tank and operation parameters have been described above. The geometrical model of the same scale stirred tank was established in Gambit 2.4.6. The whole vessel was divided into four parts to simulate impeller revolution with the Multiple Reference Frame (MRF): one rotational zone (impeller) and three static zones. Corresponding tetrahedral and hexahedral grid were employed respectively. The inner stirred zone was meshed with hybrid mesh which included tetrahedron and pyramid grids because of the irregular impeller while other three zones were meshed with structural hexahedron grids. In total, 104682 elements were generated in this process after the mesh independence tests. Fig 4 shows the global and local grid distributed on.

(Inserting Figure 4 here)

At the same time, the CFD model of electrolysis stirred device was meshed with the same generation method. Only the irregular stirred zone and conical zone were meshed with tetrahedron and pyramid while others were hexahedron. 786724 elements were generated to discrete the volume after mesh independence tests as well.

Simulations were carried out with the commercial software of Fluent 6.3. The Semi_Implicit Method for Pressure-Linked Equations (SIMPLE) scheme was adopted for pressure-velocity coupling. The standard pressure spatial discretization was selected coupling the second order upwind for spatial discretization of momentum, turbulent kinetic energy and turbulent dissipation rate. The default under relaxation factors was employed. The residual of 10^{-4} was forced on except 10^{-3} for continuity and 10^{-5} for velocity criteria. The time step size was 0.01 s.

3.3. Cold model experiment setup

Based on PIV experiments and simulation results, a 1:1 cold model of industrial lithium electrolytic cell was designed and manufactured. As is shown in Fig. 5, cathode, anode, pipes, stirring tank and collection tank were all made from polymethyl methacrylate and was installed in a glass tank. The glass tank was in size of 900×700×800mm and made from stalinite with thickness of 10mm. Liquid level was maintained 600mm during the experimental process.

According to the similarity principle, lithium was replaced by silicone oil and electrolyte was replaced by water. Silicone oil was fed to electrolytic zone. The time silicone oil cost flowing from electrolytic zone to collection zone was measured by a chronograph.

(Inserting Figure 5 here)

4. Results and Discussion

4.1. The PIV results analysis

The fluid instantaneous velocity consists of two parts: averaged velocity and fluctuating velocity. The single PIV image shows the instantaneous flow field. The measured velocity is random and unable to present the general information because of the fluctuating velocity. To obtain steady flow field, it's necessary for the images to be averaged. To find the best averaged images number, different quantities of images were averaged. The numbers of averaged images are 25, 50, 75, 100, 125, 150, 175, 200, 225, 250, 275, 300, 325, 350, 375, 400, 425, 450, 475, 500 respectively.

Fig 6.a shows the velocity vector and contour which is the averaged result of 25 pairs. To compare different averaged results, three zones were selected which were marked A, B, C in the figure. The radial averaged velocity in A, C and the axial averaged velocity in B were shown in Fig.6a. Fig 6.b shows the numerical velocity in every point with different images averaged. When 100 images were averaged, the error of velocities stayed in 3%. And the results were steady basically when the quantity of images

reached 300. These results were consistent with the literature⁴¹ which reported similar results. Hence, 300 images were selected to acquire a reliable averaged flow field for validating.

(Inserting Figure 6 here)

4.2. The validation of the CFD model

As mentioned above, different turbulent models were applied to simulate the flow field of the stirred tank. First, three kinds of k - ϵ model were tested: standard k - ϵ model, RNG k - ϵ model and realizable k - ϵ model. Fig 7.a shows the velocity contours of different k - ϵ models. It can be found that the results of different models were almost the same. The impeller generated obvious axial flow, especially in the impeller volume. It is hard to compare these models from the contours. Then, for a detailed comparison, the velocity radial distribution at different height z were treated as the comparable physical quantity, meanwhile, the location information and definitions for height Z and distance X are shown in figure 2a and figure 6a.

(Inserting Figure 7 here)

Fig 7.b shows the velocity radial distribution of different k - ϵ models at different heights. The measured velocity with PIV was also included. It was also obvious that the experimental values were close to the simulation. All of the k - ϵ models were satisfactory while the standard k - ϵ model is the simplest one to solve. Hence, by comparison, it is better to choose standard k - ϵ model.

Up to now, k - ϵ model is a typical CFD model because of its wide applicability. At the same time, more complex models are developed to simulate hard problems or improve the accuracy, like Large Eddy Simulation (LES) and Reynolds Stress Model (RSM). Each model has its own application or

advantages. The only purpose of the comparison between different models was to find the most suitable one. Fig 8 shows the comparison result between standard k- ϵ model, LES and RSM. Generally, the result of RSM agreed with the data of standard k- ϵ model and PIV well. The deviation was reasonable and acceptable. But the consuming time of RSM was longer than standard k- ϵ model during the calculation process. Thus, the standard k- ϵ model had more advantages. On the other hand, it was interesting that LES model turned out to be the worst one. From the contour, the difference of LES was clear. The flow was not symmetric and regular. The velocity distribution also demonstrated the deviation of LES. It was deduced that this may happen because the mesh size was not enough to resolve the small turbulence characteristic scales, especially the boundary layer grids⁸. Other CFD models like k- ϵ have already had a good performance in the simulations of the stirred tank. Hence, it was not worthy of simulating the LES with refined mesh because of the high computer requirement.

(Inserting Figure 8 here)

From the experiment and simulation results, it can be concluded that standard k- ϵ model, RNG k- ϵ model, realizable k- ϵ model and RSM can all simulate the stir process with acceptable error. Considering the consuming time and computational resources, standard k- ϵ model was applied in this study.

4.3. Optimization of impeller type

The stirred device is crucial to the liquid lithium collection. The axial flow which can generate a negative pressure under the impeller was expected. The type of impeller has an important effect on the flow pattern. Hence, the selection of impeller type is very significant.

Three typical types of impellers were selected for comparison: three flat blade turbine, three inclined blade turbine and propeller agitators. The last one also included four subtypes: three blades, four blades,

five blades and six blades. All of the impellers had the uniform diameter of 100 mm. It should be noticed that the height of the large pipe became 20 mm which has been optimized.

(Inserting Figure 9 here)

Flow fields with different impellers were simulated. The contours shown in Fig 9.a displayed the differences obviously. The flat blade turbine and inclined blade turbine had higher radial velocity and lower axial velocity than propeller agitators, especially the inclined blade turbine, in which condition the axial velocity in the bottom pipe was close to zero. The variations of the propeller agitators with different blades were hard to be identified from the contour. Hence, the detailed axial velocity distribution along the centre of the small pipe is shown in Fig 9.b. The result shows that the propeller agitator behaved much better. Moreover, it indicates that the axial velocity increased as the number of blades increased from three to six while the increments (4-7%) were not very large. In another word, increasing blade number was not an efficient way to improve the axial velocity. Hence, the three blades propeller agitator was selected.

4.4. Optimization of impeller diameter

Impeller diameter is an important parameter to describe any impeller. It represents the size of an impeller and its effects on the velocity field are remarkable. Different propeller agitators with three blades of diameter 60, 70, 80, 90, 100, 110, 120 and 125 mm were employed to study the effects of impeller diameter.

(Inserting Figure 10 here)

The results are shown in Fig 10. From the contours in Fig 10.a, it was obvious that the velocity in the center of the small pipe increased with the increment of impeller diameter. The detailed data in Fig 10.b also described the same conclusion. This result is related to the size of impeller swept region and the circulation in axial flow stirred device.

As is known, when the impeller rotates counterclockwise, the direct of fluid motion in the impeller swept region is upward. Then the upper fluid will move downward in the outer region because of gravity to generate a balance circulation which can be observed in Fig 10.a clearly. When the impeller diameter increased, the impeller swept region became larger and the outer region was smaller. Then the upward flow must be larger too. Compared to increase the downward flow in the outer region, it was much easier to supply the increased upward flow from the bottom small pipe in this special system. Then the axial velocity in the pipe increased with the larger required flow accordingly. To reach balance again, the fluid flowed out from the large pipe top was also increased which can be confirmed in the velocity contours.

At the same time, it should be noticed that larger stir device is not always favorable. First, the energy consumption will rise with a larger impeller. Second, with constant amount of lithium, large liquid surface means small liquid height which is hard to pump. Therefore, it is not good for the collection of liquid lithium. Third, collision will occur when the impeller is too close to the wall because of eccentric rotation in industrial operation. Hence, 100 mm impeller was selected as the optimized diameter in this study.

4.5. Optimization of impeller position

The installation of impeller has an important effect on the flow field. In chemical engineering, some impellers are even installed eccentrically to get special flow field. In this system, eccentric installation was not needed. The main concerned point was the height of impeller. In this study, the horizontal bottom of the big cylinder was defined height 0, and the upper levels had the positive height. Here, to

study the effects of impeller height which will exceed 20mm, the height of the large pipe should be changed to 200 mm to guarantee the axial flow in small pipe.

(Inserting Figure 11 here)

The height of 0, 25, 50, 75, 100, 125 and 150 mm was selected to simulate the corresponding flow fields which are shown in Fig 11.a. The height of 0 mm had obvious advantage and the velocity radial distributions in Fig 11.b display the same result. From the data comparison, the effect of impeller height on axial velocity was significant. This is easy to be understood. First, it is generally known that the effect between impeller and fluid decreased with the increment of their distance because of the fluid viscosity. Therefore, the axial velocity in small pipe must be smaller with the higher impeller. Second, the fluid which was transferred upward by impeller must be replaced by peripheral fluid which consisted of two parts: the flow from outer region and the flow from the small pipe. If the impeller was close to the small pipe, the supply fluid would be almost all from the small pipe while the outer region would be the main supplement if the impeller was far from the small pipe. In a word, the height of impeller had a significant effect on the performance of stir. The height of 0 was proper to provide maximum axial velocity.

4.6. Optimization of impeller rotational speed

As an operation parameters, the importance of impeller rotational speed is well known. Just like impeller diameter, This parameter decided the flow pattern directly because of its effect on Reynolds number. Hence, the simulations were conducted with the impeller rotational speeds of 100, 200, 300, 400 and 500 rpm. The corresponding results were shown in Fig 12.

Fig 12.a shows the velocity contours with different impeller rotational speeds. In the case of 100 rpm, the flow was weak. With the increment of impeller rotational speed, the flow got more turbulent gradually. When the impeller rotational speed reached 400 rpm, the turbulence bacame remarkable. The

magnitude of central velocity in the pipe also had a clear improvement which changed from light blue to crimson in the contours. Fig 12.b expressed the same consequence.

(Inserting Figure 12 here)

In order to validate the accuracy of CFD model in this stirred device, the PIV experiments with different impeller rotational speeds were also conducted in the collection device. The numerical simulations accorded with experimental results in general in the comparison which was shown in Fig 13, especially the results of 100 and 200 rpm. However, the velocity fluctuation in PIV results of 300 and 400 rpm should also be noticed. As mentioned above, the flow got much more turbulent when the rotational speed raised up from 100 rpm to 400rpm. In this process, fluctuating velocity also increased. The 300 averaged images which corresponding to 150 rpm was not enough for higher rotational speed. Maybe 500 pairs were suitable for 300 rpm. In a word, though parts of the PIV result were not steady, the velocity magnitude and tendency still accorded with the simulation. Hence, the consequence was still credible and the CFD model was available.

(Inserting Figure 13 here)

4.7. Cold model experiments

Velocity of the silicone oil drops varied with their positions in the pipe which were bigger in the center while smaller in the wall of the pipe. Therefore, experimental data had to be averaged to get a correct result.

Operation parameters were based on the optimization results: stirring speed being 400rpm, impeller height being 0 and stirring tank height being 20mm. Total pipe length was 710mm, so average velocity of the silicone oil in the pipe can be calculated with the time it cost in the pipe. 5 pairs of data with

different drop diameters and random positions in pipe were measured and the consumed time of the drops flowing through the whole pipe was shown in Tab 2 and the experimental setup was shown in Fig. 5.

(Inserting Table 2 here)

From the table we can see that the average velocity in the pipe was 0.17 m/s. The consuming time for the production to flow from the farthest position to the entrance of the pipe can be calculated as: $t = \pi r_{\text{cathode}} / \bar{v} = 3.14 \times 0.15 / 0.17 = 2.77s$. With the same way, when the stirring speed was 450rpm and 500rpm, the average velocity in pipe was 0.24 m/s and 0.31m/s, respectively. Thus the consuming time for the production to flow from the farthest position to the entrance of the pipe was 1.96s and 1.52s. Higher stirring speed will result in stronger turbulence in collection tank. According to the literature⁵, the time for the molten salt and Lithium to leave the electrolytic zone should better be 2s, so stirring speed can be 450rpm.

5. Conclusion

The stir device in lithium electrolysis cell which is used for liquid lithium collection was optimized. CFD was used to optimize the flow field because of the experiment difficulty of high temperature and high cost. The PIV experiments which were used to select and validate the suitable CFD model were tested in a cylinder stirred tank. Impeller type, diameter, position and rotational speed were selected as the optimized objects. A cold model of industrial lithium electrolysis cell was designed based on the optimized results and cold model experiments were carried out.

The results show that: PIV result with 300 pairs averaged had enough accuracy. Standard k-ε model was considered the best CFD model which was verified with PIV in the stirred tank. The optimization indicated that the propeller agitator had much more excellent performance than other types while the effect of impeller blade number on the velocity magnitude was not obvious. The impeller was also much better to be installed close to the small pipe. The effects of the impeller diameter and rotational speed

were significant which was related to the circulation in the flow field. High diameter and speed were expected while the feasibility of actual operation should be noticed. CFD turbulent single phase model is effective for stirring system for its medium angle speed and low velocity.

■ Author Information

Corresponding Author

*Telephone: 86-21-64250981. Fax: 86-21-64250981. E-mail: zsun@ecust.edu.cn.

■ Acknowledgment

We acknowledge the financial support provided by the National Natural Science Foundation of China (Grant 21206038), the Specialized Research Fund for the Doctoral Program of Higher Education (New Teachers) (Grant 20120074120014).

■ References

- [1] J. A. Epstein, E. M. Feist, J. Zmora. Extraction of lithium from the dead sea [J]. Chem. Eng. Sci., 1981, 6(3): 269-275.
- [2] Donald R. Sadoway. Toward new technologies for the production of lithium [J]. JOM. 1998, 50(5): 24-26.
- [3] William A. Averill, David L. Olson. A review of extractive processes for lithium from ores and brines [J]. Chem. Eng. Sci., 1978, 3(3):305-313.
- [4] Albert Brut, Gérard Nave, Jean Pierre, et. Electrolyzer and a method for the production of readily oxydizable metals in a state of high purity [P]. USA: US3962064, 1986.
- [5] Jürgen Müller K. Process and apparatus for producing high-purity lithium metals by fused-salt electrolysis [P]. USA: US4740279, 1988.

- [6] Jean-Michel Verdier. Continuous electrolysis of lithium chloride into lithium metal [P]. USA: US4617098, 1986.
- [7] John D. Anderson. Computational fluid dynamics the basic with applications [M]. McGraw-Hill, 1995:3-7.
- [8] J. Gimbun, C. D. Rielly, Z. K. Nagy, et. Detached eddy simulation on the turbulent flow in a stirred tank [J]. *AIChE*, 2012, 58(10): 3224-3241.
- [9] D.A. Deglon, C.J. Meyer. CFD modelling of stirred tanks: Numerical considerations. *Minerals Engineering* 19 (2006) 1059–1068.
- [10] Koh, P.T.L., Schwarz, M.P., 2005. CFD Modelling of bubble-particle attachments in a flotation cell. In: *Proc. Centenary of Flotation Symposium, Brisbane*, pp. 201–207.
- [11] Koh, P.T.L., Schwarz, M.P., Zhu, Y., Bourke, P., Peaker, R., Franzidis, J.P., 2003. Development of CFD models of mineral flotation cells. In: *Proc. Third International Conference on CFD in the Minerals and Process Industries, Melbourne*, pp. 171–175.
- [12] Maoming Gong, Chunshan Li and Zengxi Li. Numerical analysis of flow in a highly efficient flotation column. *Asia-Pac. J. Chem. Eng.* 2015, 10: 84-95
- [13] Alvin W. Nienow, David Miles. Impeller power numbers in closed vessels [J]. *Ind. Eng. Chem. Process Des. Develop.*, 1971, 10(1): 41-43.
- [14] K. Rutherford, S. M. Mahmoudi, K. C. Lee, etc. The influence of Rushton impeller blade and disk thickness on the mixing characteristics of stirred vessels [J]. *Chem. Eng. Res & Des.*, 1996, 74(3): 369-378.
- [15] M. B. Machado, J. R. Nunhez, D. Nobes, etc. Impeller characterization and selection: balancing efficient hydrodynamics with process mixing requirements [J]. *AIChE*, 2011, 00(0): 1-16.
- [16] Genwen Zhou, Suzanne Kresta. Impact of tank geometry on the maximum turbulence energy dissipation rate for impellers [J]. *AIChE*, 1996, 42(9): 2476-2490.

- [17] Hartmann, H., Derksen, J.J., Montavon, C., Pearson, J., Hamill, I.S., Van den Akker, H.E.A., 2004. Assessment of large eddy and RANS stirred tank simulations by means of LDA. *Chemical Engineering Science* 59, 2419-2432.
- [18] Eggels, J.M.G., 1996. Direct and large eddy simulations of the turbulent fluid flow using the lattice-Boltzman scheme. *International Journal of Heat and Fluid Flow* 17, 307-323.
- [19] D.M. Hargreaves, N.G. Wright. On the use of the k- ϵ model in commercial CFD software to model the neutral atmospheric boundary layer. *Journal of Wind Engineering and Industrial Aerodynamics* 95 (2007) 355–369
- [20] Ranade, V.V., Joshi, J.B., & Marathe, A.G. (1989). Flow generated by pitched blade turbines II: Simulation using k-e model. *Chem. Eng. Comm.* 81, 225-248.
- [21] Abujelala, M.T., Lilley, D.G., 1984. Limitations and empirical extensions of the k-e model as applied to turbulent confined swirling flows. *Chemical Engineering Communications* 31, 223–236.
- [22] Armentante, P.M., Luo, C., Chou, C., Fort, I., Medek, J., 1997. Velocity profiles in a closed vessel: comparison between experimental LDV data and numerical CFD predictions. *Chemical Engineering Science* 52, 3483-3492.
- [23] Jenne, M., Reuss, M., 1999. A critical assessment on the use of k-e turbulence models for simulation of the turbulent liquid flow induced by a Rushton-turbine in a baffled stirred-tank reactor. *Chemical Engineering Science* 54, 3921-3942.
- [24] Jaworski, Z., Zakrzewska, B., 2002. Modelling of the turbulent wall jet generated by a pitched blade turbine impeller: the effect of turbulence model. *Transactions of IChemE* 80, 846-854.
- [25] R. Krishna, J. M. Van Baten, J. Ellenberger, etc. CFD simulations of sieve tray hydrodynamics [J]. *IChemE*, 1999, 77: 639-646.
- [26] Christian Drumm, Menwer M. Attarakih, H.-J. Bart. Coupling of CFD with PBM for an RDC extractor [J]. *Chem. Eng. Sci.*, 2009, 64: 721-732.

- [27] A. Shahmohammadi, A. Jafari. Application of different CFD multiphase models to investigate effects of baffles and nanoparticles on heat transfer enhancement. *Front. Chem. Sci. Eng.*, 2014, 8 (3): 320-329
- [28] Minhua Zhang, Fang Meng, Zhongfeng Geng. CFD simulation on shell-and-tube heat exchangers with small-angle helical baffles [J]. *Front. Chem. Sci. Eng.*, DOI: 10.1007/s11705-015-1510-x
- [29] W. Y Fei, Y. D. Wang, Y. K. Wan. Physical modelling and numerical simulation of velocity field in rotating disc contactor via CFD simulation and LDV measurement [J]. *Chem. Eng. J.*, 2000, 78: 131-139.
- [30] M. W. Hlawitschka, H.-J. Bart. Determination of local velocity, energy dissipation and phase fraction with LIF- and PIV- measurement in a Kuhni miniplant extraction column [J]. *Chem. Eng. Sci.*, 2012, 69: 138-145.
- [31] S. Baldi, A. Ducci, M. Yanneskis. Determination of dissipation rate in stirred vessels through direct measurement of fluctuating velocity gradients [J]. *Chem. Eng. Technol.*, 2004, 27(3): 275-281.
- [32] R. J. Adrian. Twenty years of particle image velocimetry [J]. *Exp. Fluids*, 2005, 39: 159-169.
- [33] J. Kilander, A. Rasmuson. Energy dissipation and macro instabilities in a stirred square tank investigated using an LE PIV approach and LDV measurements [J]. *Chem. Eng. Sci.*, 2005, 60: 6844-6856.
- [34] Sagar S. Deshpande, Mayur J. Sathe, Jyeshtharaj B. Joshi. Evaluation of local turbulent energy dissipation rate using PIV in jet loop reactor [J]. *Ind. Eng. Chem. Res.*, 2009, 48: 5046-5057.
- [35] J. Sheng, H. Meng, R. O. Fox. A large eddy PIV method for turbulence dissipation rate estimation [J]. *Chem. Eng. Sci.*, 2000, 55: 4423-4434.
- [36] Christian Drumm, Mark W. Hlawitschka, H.-J. Bart. CFD simulations and particle image velocimetry measurements in an industrial scale rotating disc contractor [J]. *AIChE*, 2011, 57(1): 10-26.
- [37] D. F. Hill, K. V. Sharp, R. J. Adrian. Stereoscopic particle image velocimetry measurements of the flow around a Rushton turbine [J] *Exp. Fluids*, 2000, 29(5): 478-485.

[38] Pianko-Oprych P, Nienow AW, Barigou M. Positron emission particle tracking (PEPT) compared to particle image velocimetry (PIV) for studying the flow generated by a pitched-blade turbine in single phase and multi-phase systems[J]. Chemical Engineering Science, 2009,64(23): 4955-4968.

[39] Deshpande SS, Sathe MJ, Joshi JB. Evaluation of local turbulent energy dissipation rate using PIV in jet loop reactor[J]. Industrial & Engineering Chemistry Research, 2009,48(10): 5046-5057.

[40] Khan FR, Rielly CD, Brown DAR. Angle-resolved stereo-PIV measurements close to a down-pumping pitched-blade turbine[J]. Chemical Engineering Science, 2006,61(9): 2799-2806.

[41] K.V. Sharp. PIV study of small-scale flow structure [J]. AIChE, 2001, 47(4): 766-778.

Table 1. The geometry parameters of the stirred device in electrolysis cell.

Table 2. Velocity in the tube

Figure 1. The structural diagram of lithium electrolysis cell.(1-Observing hole, 2-Wall of electrolysis cell, 3-Surface of liquid electrolysis, 4-Anode, 5-Cathode, 6-Chloride collector, 7-Axes of impeller, 8-Liquid lithium, 9-Impeller)

Figure 2. Cross-sectional view of vessels: (a) the validation stirred tank; (b) the simplified electrolysis stirred device.

Figure 3. The schematic diagram of the PIV system

Figure 4. The mesh of validation model (a) The global grid distribution; (b) the cross section view of the grid distribution.

Figure 5 The cold model of the lithium electrolyzer

Figure 6 The effect of the averaged images number on the velocity field. (a) The averaged velocity field of the stirred tank with 25 instantaneous images. (b) The effect of the averaged images number on the velocity.

Figure 7 Turbulence model comparison (a) Velocity contours of standard k- ϵ model, RNG k- ϵ model and realizable k- ϵ model from left to right. (b) Velocity radial distribution of various k- ϵ model at the height of 100, 110 and 120 mm from left to right

Figure 8 Turbulence model comparison (a) Velocity contours of standard k- ϵ model, RSM model and LES model from left to right. (b) Velocity radial distribution of various turbulence model at the height of 100, 110 and 120 mm from left to right

Figure 9 Effects of impeller types (a) Velocity contours of three flat blade turbine, three inclined blade turbine and propeller agitators with three, four, five and six blades from left to right.(b) Velocity radial distribution of three flat blade turbine, three inclined blade turbine and propeller agitators with three, four, five and six blades from left to right.

Figure 10 Effects of impeller diameters (a) Velocity contours of different diameter which increases from left to right (b) Velocity radial distribution of different diameter.

Figure 11 Effects of impeller installed height (a) Velocity contours of different impeller height which increases from left to right. (b) Velocity radial distribution of different impeller height

Figure 12 Effects of impeller speed (a) Velocity contours of different impeller rotational speeds which increases from left to right (b) Velocity radial distribution of different impeller rotational speeds.

Figure 13 Comparison between the PIV and simulation of the maximum central velocity with different impeller rotational speeds.

Table 1. The geometry parameters of the stirred device in electrolysis cell.

Physical quantities	value (mm)
Side length of the square vessel T	250
Diameter of the large cylinder T1	140
Diameter of the small cylinder T2	40
Height of the water in the square vessel H	550
Height of the large pipe H1	200
Height of the transition pipe H2	55
Height of the small pipe H3	100

Table 2. Velocity in the tube

No.	1	2	3	4	5	Average
Consumed time (s)	3.72	4.47	3.85	4.09	4.63	4.15
velocity (m/s)	0.19	0.16	0.18	0.17	0.15	0.17

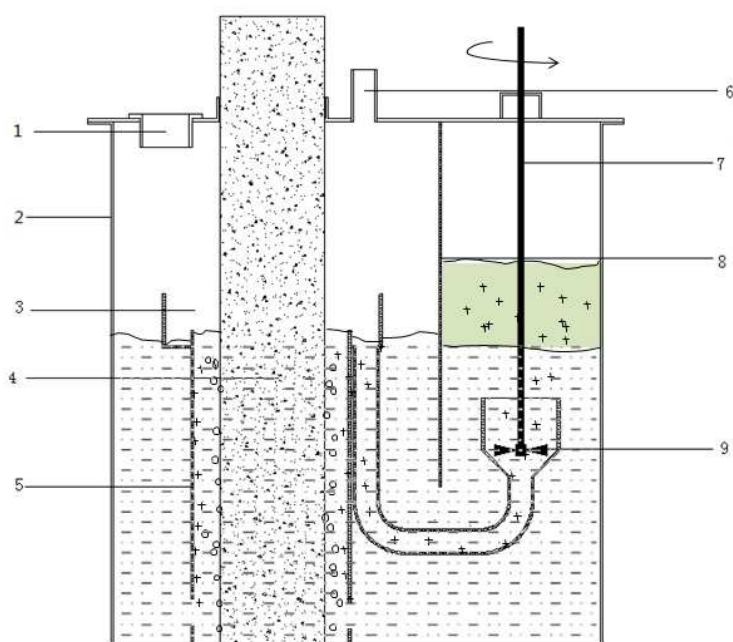


Figure 1. The structural diagram of lithium electrolysis cell.(1-Observing hole, 2-Wall of electrolysis cell, 3-Surface of liquid electrolysis, 4-Anode, 5-Cathode, 6-Chloride collector, 7-Axes of impeller, 8-Liquid lithium, 9-Impeller)

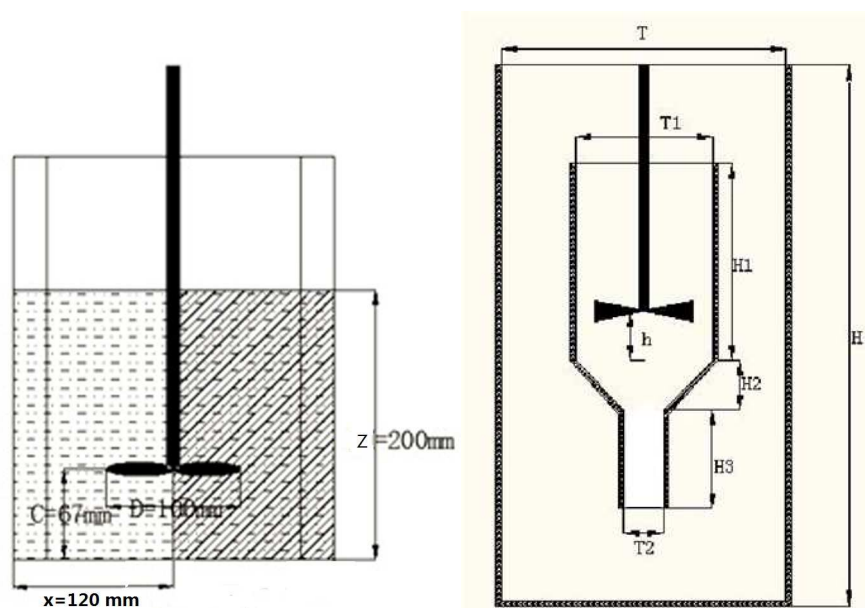


Figure 2. Cross-sectional view of vessels: (a) the validation stirred tank; (b) the simplified electrolysis stirred device.

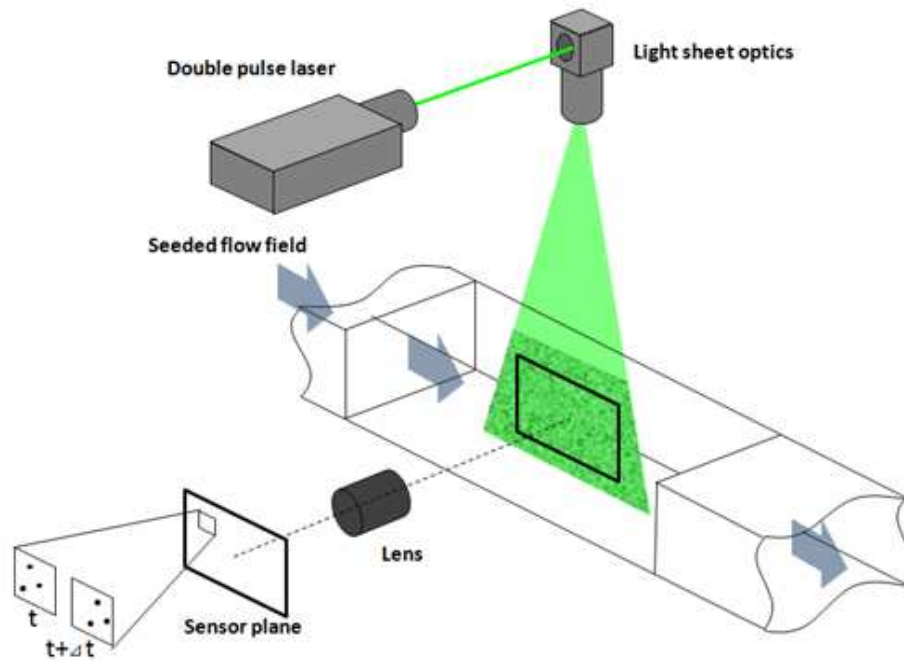


Figure 3. The schematic diagram of the PIV system

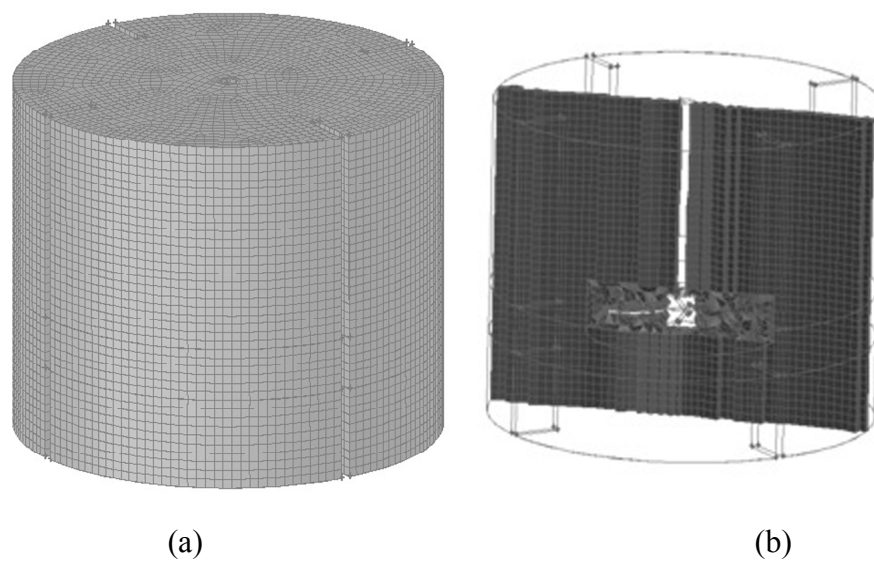


Figure 4. The mesh of validation model (a) The global grid distribution; (b) the cross section view of the grid distribution.

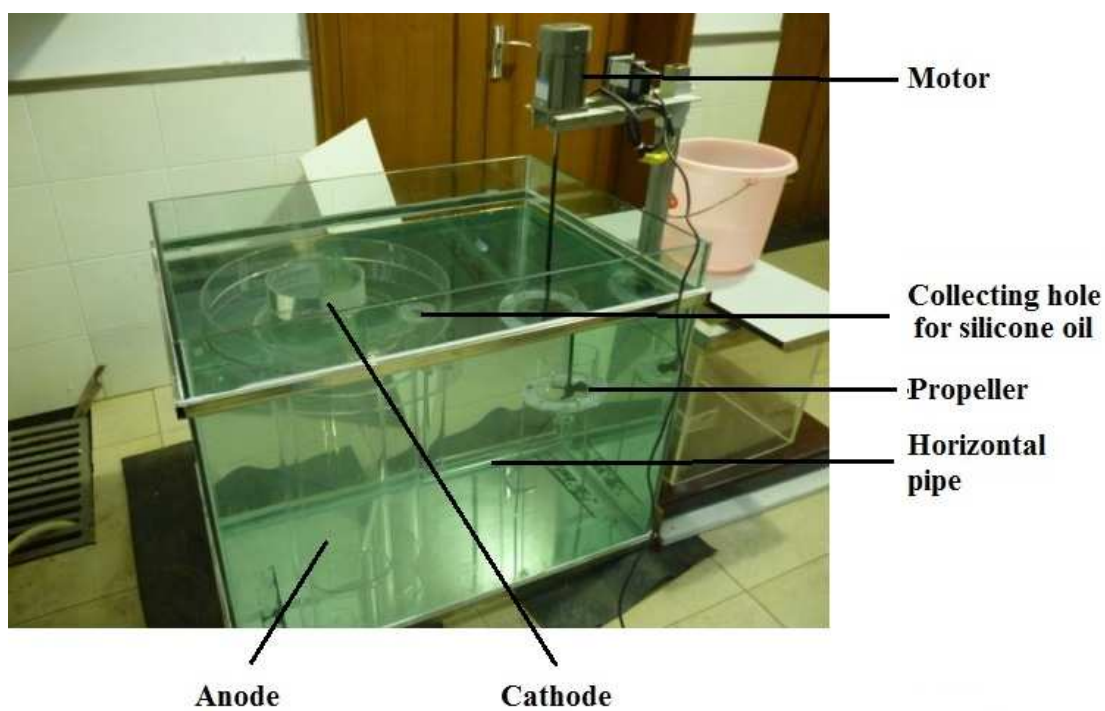
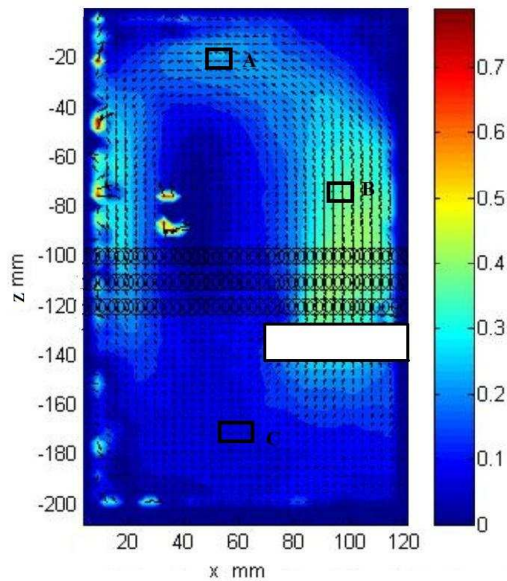
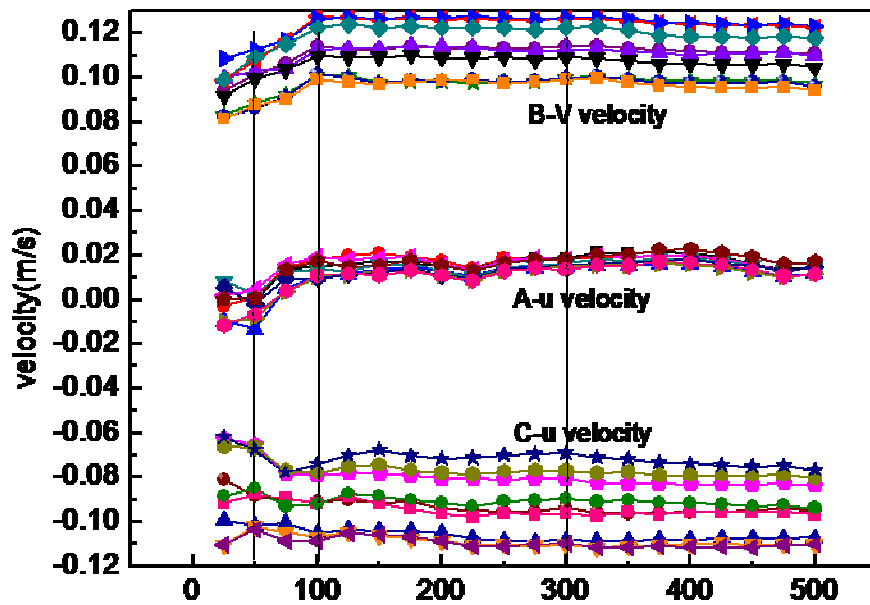


Figure 5 The cold model of the lithium electrolyzer

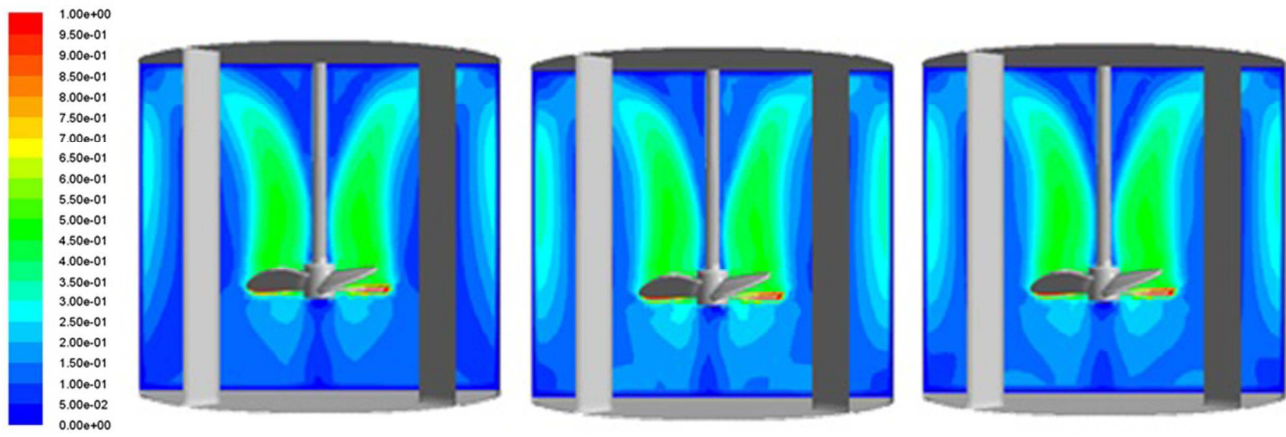


(a)

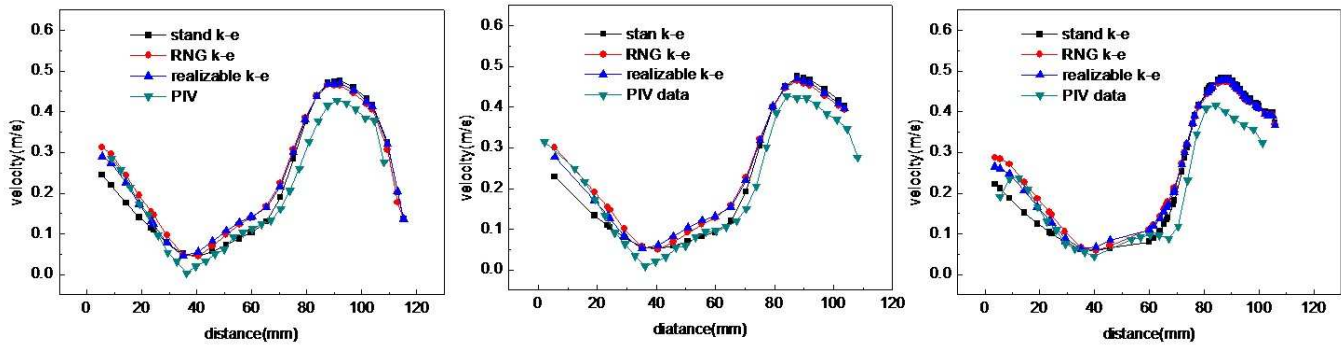


(b)

Figure 6 The effect of the averaged images number on the velocity field. (a) The averaged velocity field of the stirred tank with 25 instantaneous images. (b) The effect of the averaged images number on the velocity.

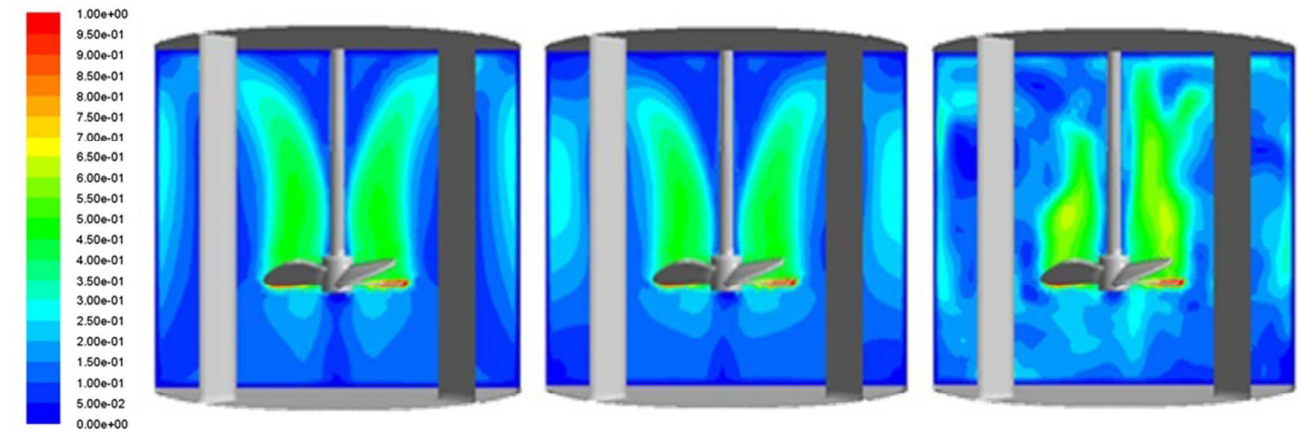


(a)

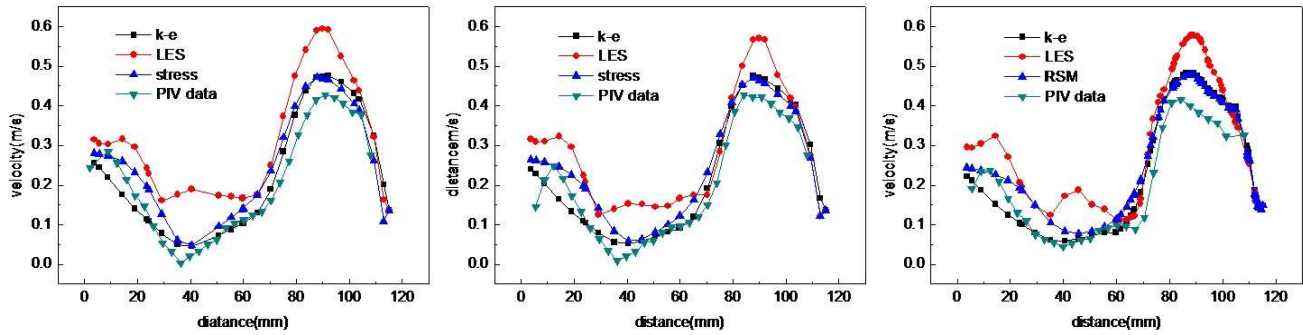


(b)

Figure 7 Turbulence model comparison under k- ϵ series (a) Velocity contours of standard k- ϵ model, RNG k- ϵ model and realizable k- ϵ model from left to right. (b) Velocity radial distribution of various k- ϵ model at the height of 100, 110 and 120 mm from left to right

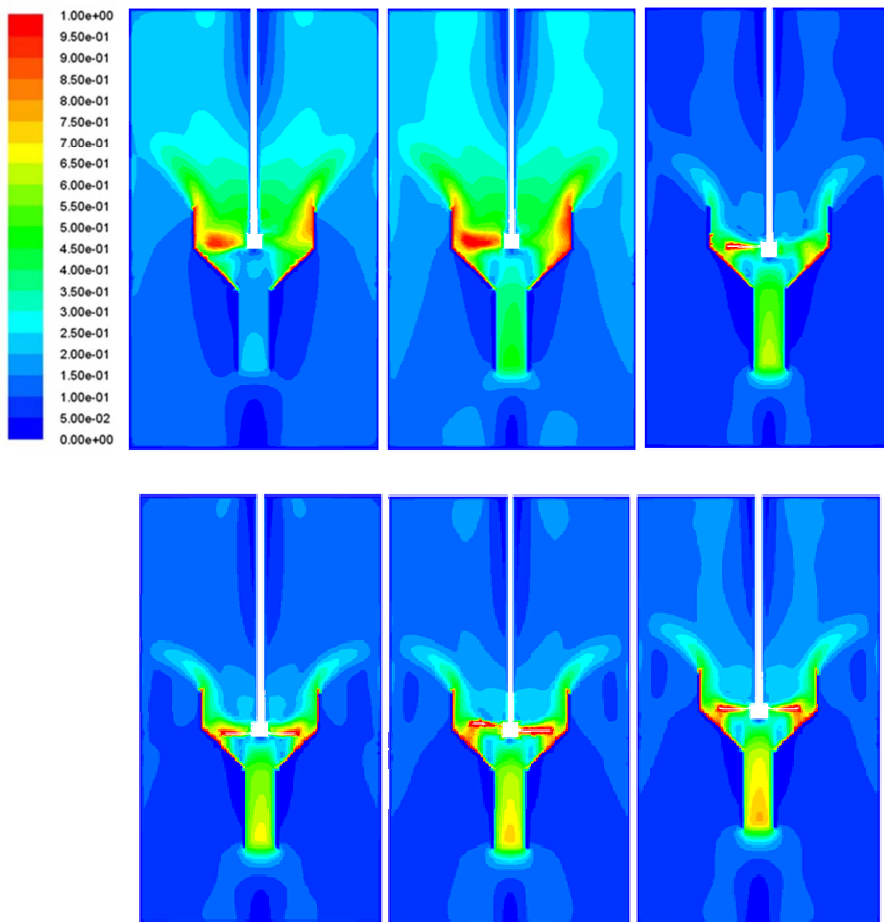


(a)

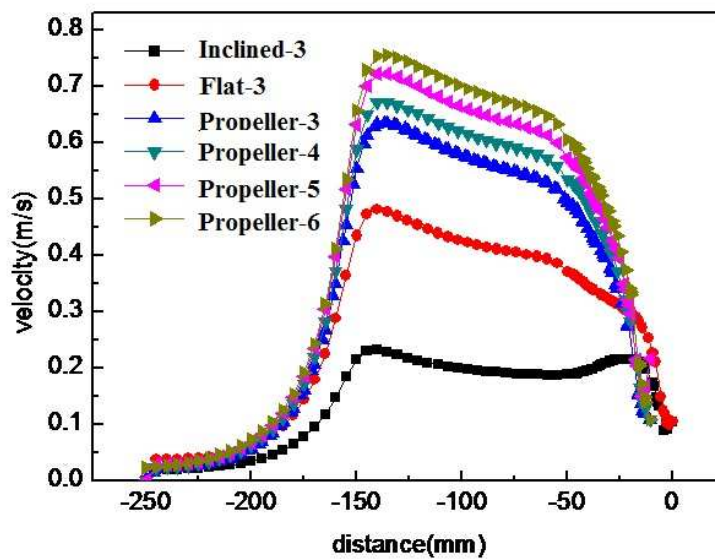


(b)

Figure 8 Turbulence model comparison (a) Velocity contours of standard $k-\epsilon$ model, RSM model and LES model from left to right. (b) Velocity radial distribution of various turbulence model at the height of 100, 110 and 120 mm from left to right

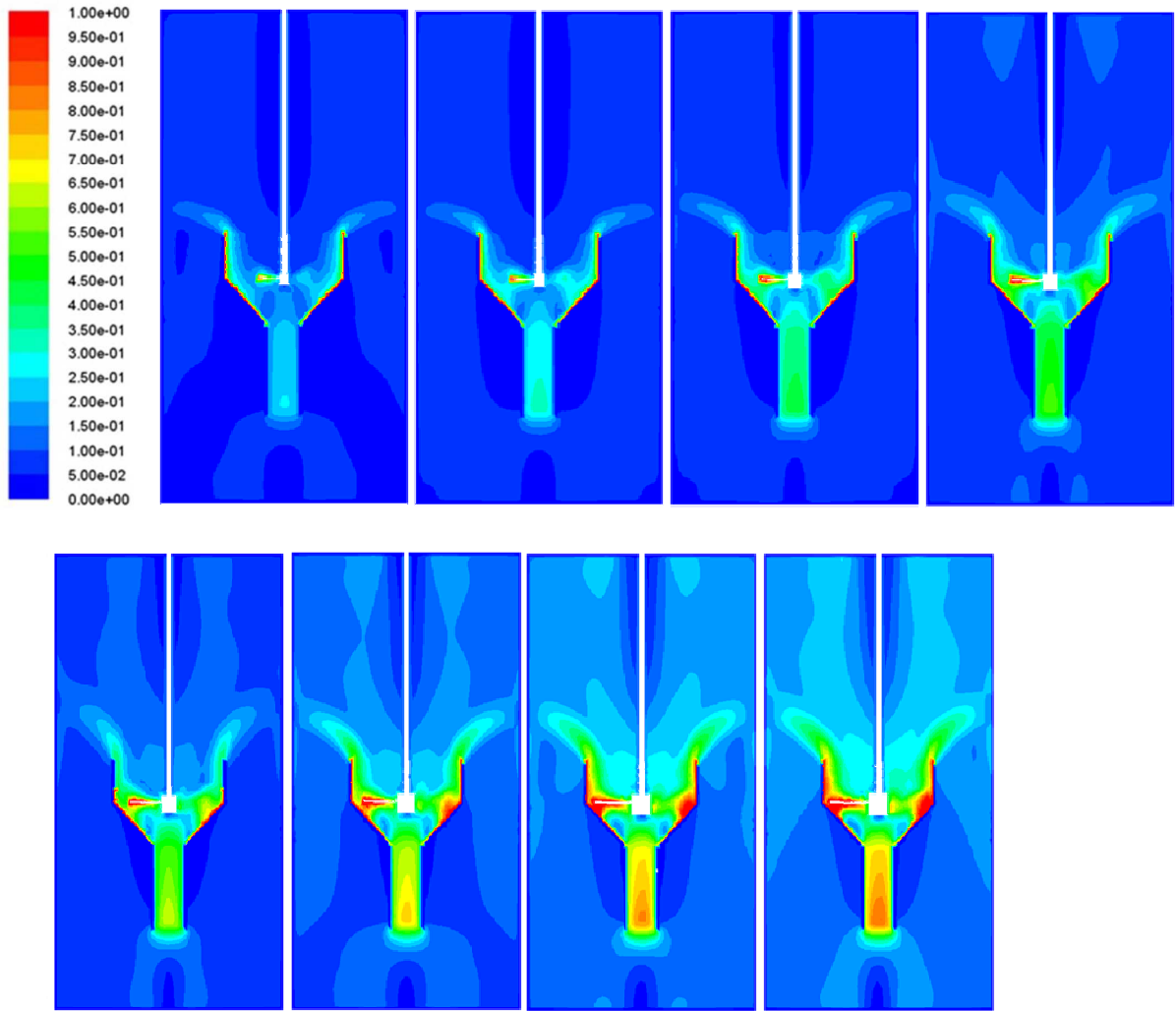


(a)

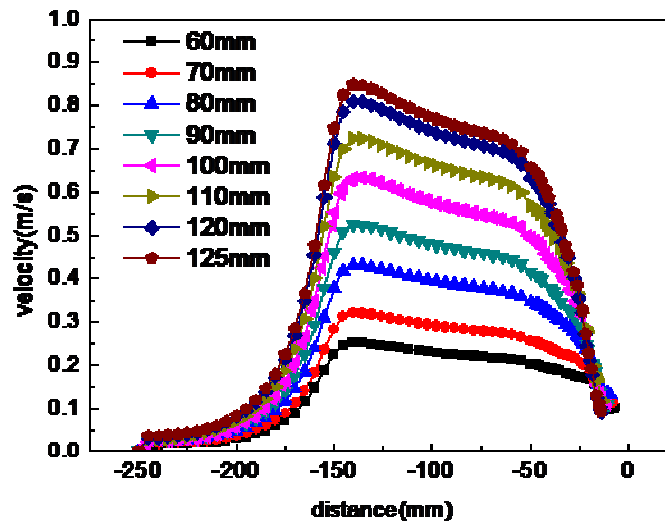


(b)

Figure 9 Effects of impeller types (a) Velocity contours of three flat blade turbine, three inclined blade turbine and propeller agitators with three, four, five and six blades from left to right.(b) Velocity radial distribution of three flat blade turbine, three inclined blade turbine and propeller agitators with three, four, five and six blades from left to right.

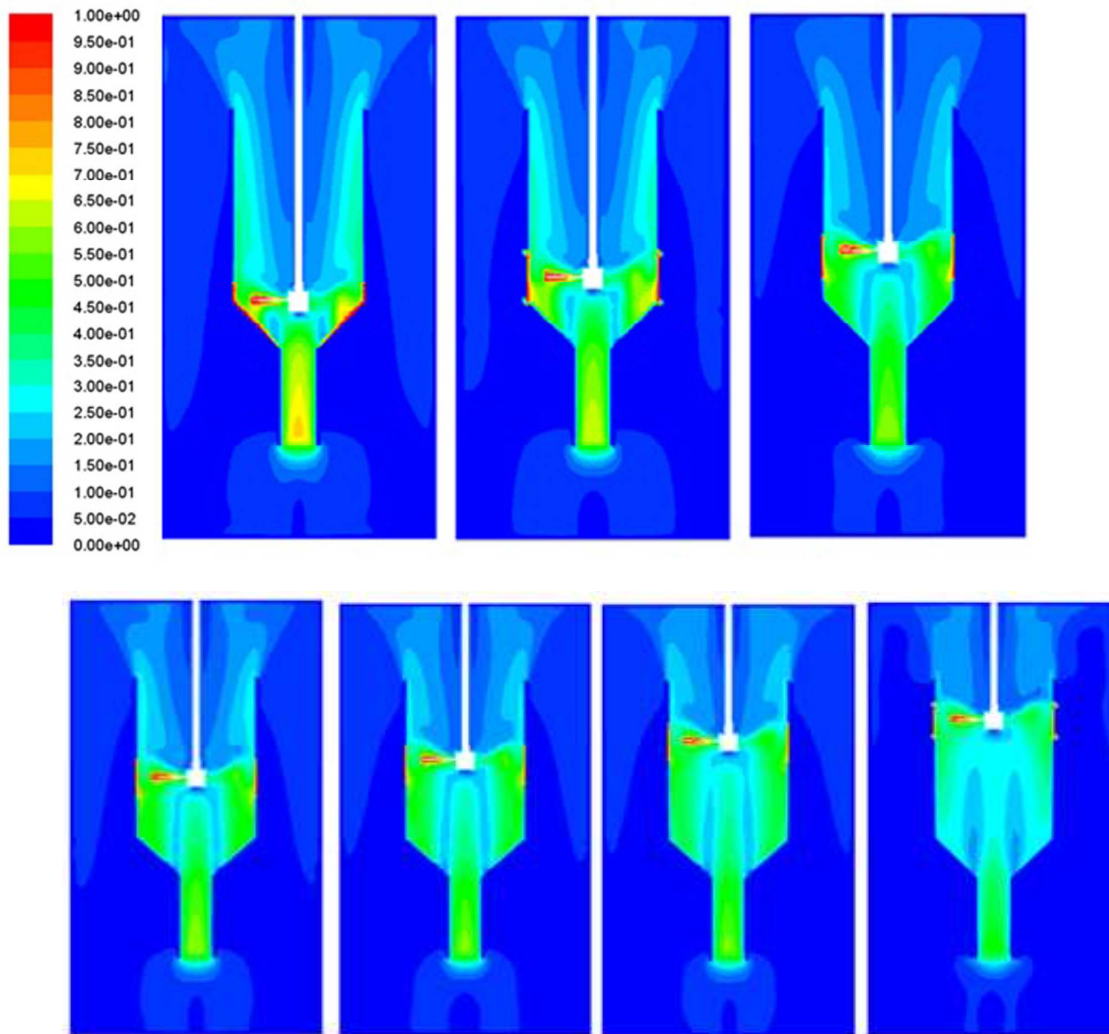


(a)

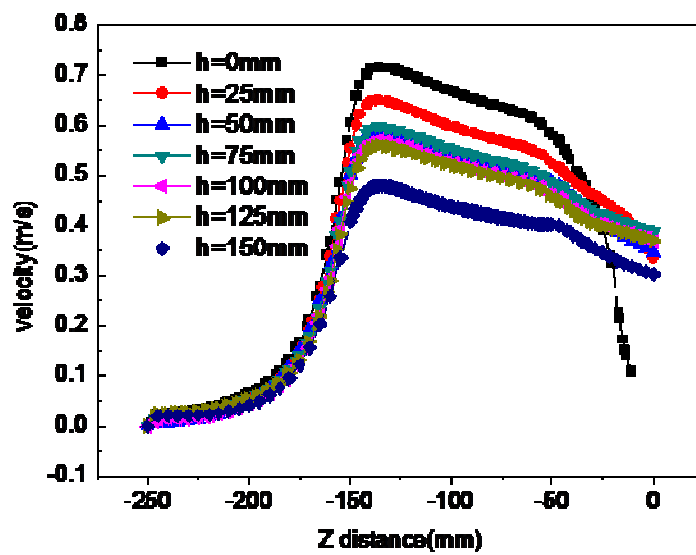


(b)

Figure 10 Effects of impeller diameters (a) Velocity contours of different diameter which increases from left to right (b) Velocity radial distribution of different diameter.

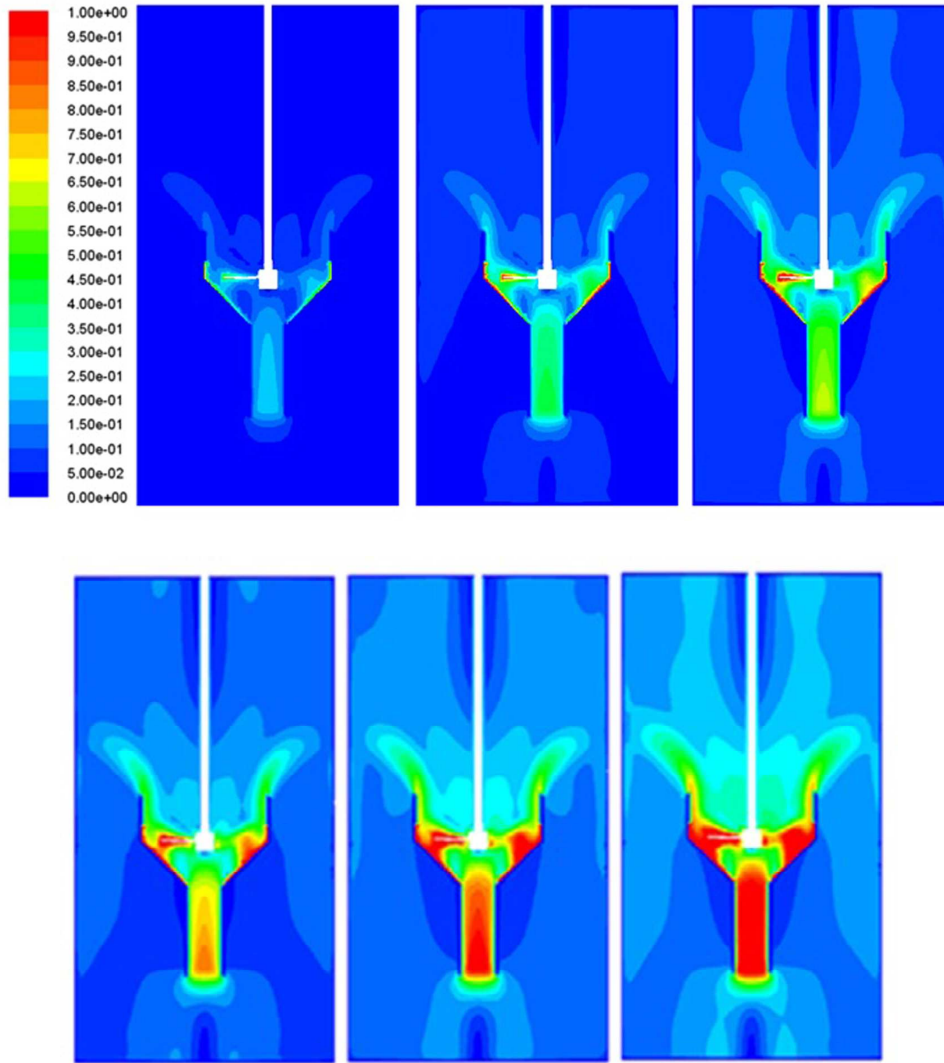


(a)



(b)

Figure 11 Effects of impeller installed height (a) Velocity contours of different impeller height which increases from left to right. (b) Velocity radial distribution of different impeller height



(a)

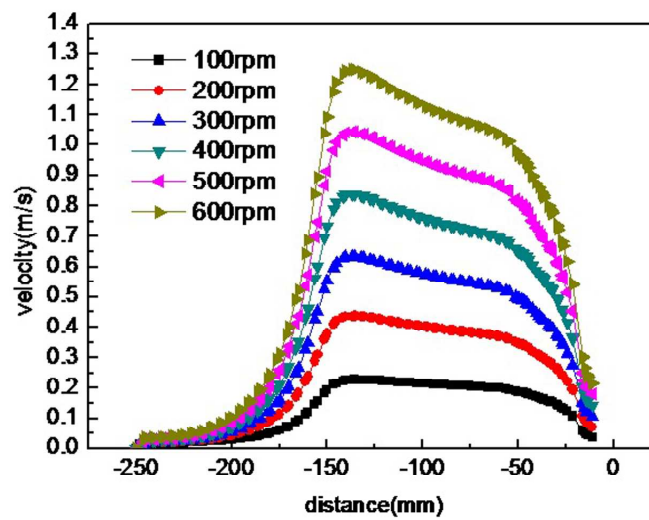


Figure 12 Effects of impeller speed (a) Velocity contours of different impeller rotational speeds which increases from left to right (b) Velocity radial distribution of different impeller rotational speeds.

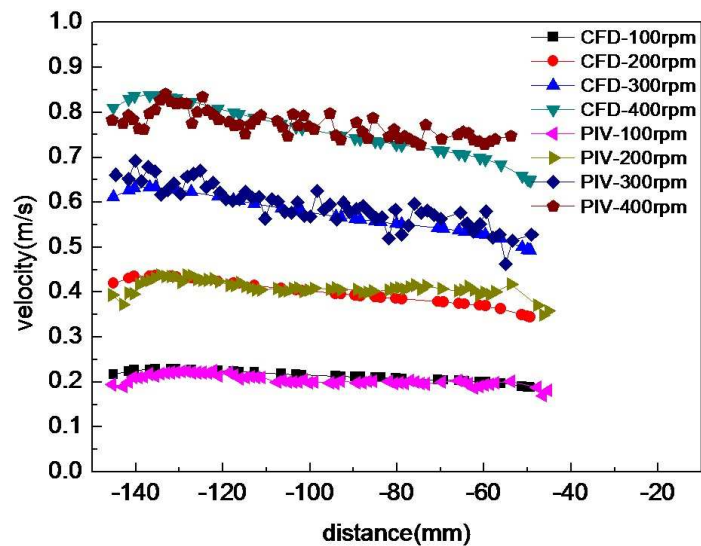


Figure 13 Comparison between the PIV and simulation of the maximum central velocity with different impeller rotational speeds.